Supporting information for:

Nano-Propellers and their Actuation in Complex Viscoelastic Media

Debora Schamel[a,b], Andrew G. Mark[b], John G. Gibbs[a], Cornelia Miksch[a], Konstantin I. Morozov[c], Alexander M. Leshansky[c], and Peer Fischer[a,b*]

[a] *Max Planck Institute for Intelligent Systems, Heisenbergstr. 3, 70569 Stuttgart, Germany*

[b] *Institute for Physical Chemistry, University of Stuttgart, Pfaffenwaldring 55, 70569 Stuttgart, Germany*

[c] *Department of Chemical Engineering and Russell Berrie Nanotechnology Institute, Technion, Haifa 32000, Israel*

E-mail: fischer@is.mpg.de

*To whom correspondence should be addressed

Surface Chemistry

To verify that chemical interaction does not account for the large differences in micro- and nano-helices propulsion in hyaluronan gels, we performed the same QD-functionalization on a reference sample of the micro-propellers as was done for the nano-screws. In 5 mg/mL HA solution, a few of these functionalized micro-screws were actually observed to propel, albeit very slowly, while the majority of particles still appeared stuck in the gel. The highest speed observed amounted to about 0.5μm/s (dimensionless velocity 0.06), on average they moved at 0.11 $\pm$ 0.12 μm/s. This corresponds to a dimensionless velocity of about 0.01, which is still very low compared to the nano-helices. We therefore attribute the very high velocities observed in the nano-propellers to a size- rather than a surface interaction effect.

Effect of the thermal noise on propulsion of externally actuated nanomotors

Let us consider the synchronous high-frequency propulsive regime[1], *i.e.* the nanohelix forming a stable angle θ with the field rotation axis Z, undergoing wobbling/precession synchronously with the field (the fastest possible frequency is the step-out frequency) and propelling along the axis of the field rotation with velocity $\mathcal{U}_Z$ (for notation see Ref. S1). Typically some low value of the precession angle, e.g. $\theta \approx 5^\circ$, is considered as the wobbling-to-swimming transition threshold.[S2 1]

The thermal noise may affect the propulsion of a nanomotor in three different ways: (i) hindering the forced rotation about the helical axis effectively reducing Ω_3 (*i.e. via* rotational diffusion *about* the helical axis, $D_r^{\parallel}$); (ii) hindering directionality/steerability by altering the precession angle θ between the helical axis and the direction of the field rotation

[1]High-frequency sync regime corresponds to $A < \omega < \omega_{s-o}$ where $\omega_{s-o} = \sqrt{A^2 + C^2}$ is the step-out frequency with $A = m_{\parallel} H/\kappa_{\perp}$ and $C = m_{\perp} H/\kappa_{\parallel}$ being the characteristic frequencies of the problem; it is characterized by a steady precession/wobbling angle $0 < \theta < \pi/2$, such that $s_\theta = A/\omega$ (see[S1] for details).

(*via* rotational diffusion *of* the helical axis, $D_r^{\perp}$) and (iii) hindering forward propulsion (*via* translational diffusion along the Z-axis, D_t).

All the above mechanisms are characterized by their respective Péclet numbers (Pe) that compare the relative importance of the external forcing and noise. The simple scaling criterion for the minimal size of the nanomotor can be derived from the condition Pe = 1, *i.e.* when thermal and external forces are equally important. Note that the mechanisms (i) and (iii) directly affect the forward propulsion, while (ii) affects directionality/steerability of the nanomotor. The proper Pe's for the mechanisms (i) and (iii) are, respectively

$$\mathrm{Pe}_r^{\parallel} = \frac{\Omega_3}{D_r^{\parallel}}\,, \qquad \mathrm{Pe}_t = \frac{\mathcal{U}_Z L}{D_t}\,. \tag{S1}$$

where $D_r^{\parallel} = \kappa_B T/\kappa_{\parallel}$ is a rotational (about the symmetry axis) self-diffusion coefficient, $D_t = \kappa_B T/(\xi_{\parallel} c_\theta^2 + \xi_{\perp} s_\theta^2)$ - translational diffusivity (along the Z-axis), with $\kappa_{\parallel}$ being the viscous rotational resistance of the helix (*i.e.* to rotation about the symmetry axis) and $\xi_{\parallel}$ and $\xi_{\perp}$ are the corresponding translational viscous resistance (along and perpendicular to the helical axis, respectively).

The angular velocity of the propeller about the helical axis in the high-frequency sync regime reads[S1] $\Omega_3 = \dot{\varphi} c_\theta + \dot{\psi} = \omega c_\theta = \omega\sqrt{1 - A^2/\omega^2}$. The rotational resistance coefficient $\kappa_{\parallel}$ of the helix of length L can in general be re-written

$$\kappa_{\parallel} = \widetilde{\kappa}_{\parallel} \eta L^3\,, \tag{S2}$$

where η is the dynamic viscosity of the liquid, $\widetilde{\kappa}_{\parallel}$ is the dimensionless resistance.

Thus from the condition $Pe_r^{\parallel} = 1$, substituting $\kappa_{\parallel}$ from (S2) we obtain the critical length of the helix where noise and external driving are equally important,

$$L_{r*}^{\parallel} = \left(\frac{\kappa_B T}{\widetilde{\kappa}_{\parallel}\eta\omega c_\theta}\right)^{1/3} \simeq \left(\frac{\kappa_B T}{\widetilde{\kappa}_{\parallel}\eta\omega}\right)^{1/3}\,, \tag{S3}$$

where the last equality holds for small wobbling angles θ.

Analogously, for the mechanism (iii) the propulsion speed of the nanohelix in high-frequency sync regime is $\mathcal{U}_Z = -\omega c_\theta^2 \mathcal{B}_\parallel/\xi_\parallel = -\omega(1 - A^2/\omega^2)\mathcal{B}_\parallel/\xi_\parallel$, where $\mathcal{B}_\parallel$ is the coupling viscous resistance coefficient [2]. This coefficient scales as $\mathcal{B}_\parallel = \widetilde{\mathcal{B}}_\parallel \eta L^2$, where again the dimensionless coefficient $\widetilde{\mathcal{B}}_\parallel$ depends solely on the geometry. Thus, the condition $\mathrm{Pe}_t = 1$ yields

[2]

$$L_{t*} = \left(\frac{\kappa_B T}{\widetilde{\mathcal{B}}_\parallel \eta \omega c_\theta^2 (c_\theta^2 + \gamma s_\theta^2)}\right)^{1/3} \simeq \left(\frac{\kappa_B T}{\widetilde{\mathcal{B}}_\parallel \eta \omega}\right)^{1/3}, \tag{S4}$$

where $\gamma = \xi_\perp/\xi_\parallel$ is typically in the range 1.2 – 1.5[3] and the last equality holds for small wobbling angles θ. For example, for $\theta = 20^\circ$ and $\gamma = 1.5$ we already have $[c_\theta^2(c_\theta^2 + \gamma s_\theta^2)]^{-1/3} \simeq 1.023$. Thus, both mechanisms (i) and (iii) possess the same scaling $L_* \sim (\kappa_B T/\eta\omega)^{1/3}$ up to a multiplicative dimensionless geometric factor, *i.e.* $\widetilde{\kappa}_\parallel^{-1/3}$ and $\widetilde{\mathcal{B}}_\parallel^{-1/3}$. Note that in deriving Eq. (S4) we assumed that the frequency of the forced rotation of the nanohelix is ω, *i.e.* is not affected by the thermal noise, while in reality it is $\omega' < \omega$ due to mechanism (i). Therefore, S4 gives a lower estimate of the propeller's minimal size.

[3]

The mechanism (ii) responsible for steerability is less obvious than the other two, as it concerns perturbation the precession angle θ. Altering θ also affects indirectly the propulsion speed $\mathcal{U}_Z$ and angular velocity Ω_3. Steerability can be quantified by the ratio between the typical diffusion time driving the helix away from stable precession angle θ, *i.e.* $\tau_d \sim 1/D_r^\perp$, whereas $D_r^\perp = \kappa_B T/\kappa_\perp$ is a rotational diffusion coefficient OF the helical symmetry axis (*i.e.* defined by the auto-correlation $\langle\theta(0)\theta(t)\rangle = 2D_r^\perp t$), and the typical *relaxation* time, τ_{rel} of the helix towards θ.

[2] We consider here, for simplicity, chirality *along* the axis, *i.e.* , that in the body-fixed coordinate frame the only non-zero component of $\boldsymbol{\mathcal{B}}$ is $\mathcal{B}_\parallel$. In general there is non-negligible off-diagonal component of $\boldsymbol{\mathcal{B}}$ resulting in drift in tumbling regime.

[3] Approximating the propeller by a prolate spheroid, we have $\gamma = 2\left(\frac{1-E/2}{1+E/2}\right) + \mathcal{O}(\epsilon^2 \ln \epsilon)$, where $E = (\ln 2/\epsilon)^{-1}$ and $\epsilon = b/a < 1$ is the aspect ratio; for $\epsilon = 0.25 \div 0.05$ we have $\gamma \approx 1.22 \div 1.52$.

The typical relaxation time of the helix towards the steady angle θ can be found by considering the dynamics of a small perturbation (primed variables) of a high-frequency steady-state solution

$$\theta \to \theta + \theta' \, , \psi \to \psi + \psi' \, , \widetilde{\varphi} \to \widetilde{\varphi}' \, ,$$

where it was previously found that $s_\theta = A/\omega$, $s_\psi = -(\omega/C)c_\theta = -\sqrt{\omega^2 - A^2}/C$. Substituting this into the equations governing the dynamics (Eqs. 6-8 in [S1]) we find

$$-B\widetilde{\varphi}' c_\psi s_\theta = \omega\theta' + \dot{\widetilde{\varphi}}' s_\theta \, , \tag{S5}$$

$$A\widetilde{\varphi}' c_\theta + B\widetilde{\varphi}' s_\psi s_\theta = \dot{\theta}' \, , \tag{S6}$$

$$-C(\widetilde{\varphi}' c_\psi + \widetilde{\varphi}' c_\psi c_\theta) = \dot{\widetilde{\varphi}}' c_\theta + \dot{\psi}' \, . \tag{S7}$$

Here $A = m_\parallel H/\kappa_\perp$, $B = m_\perp H/\kappa_\perp$, and $C = m_\perp H/\kappa_\parallel$ are the three characteristic frequencies of the problem. The first two Eqs. (S5–S6) decouple from Eq. (S7). To study the dynamics of coupled perturbations $\widetilde{\varphi}'(t)$ and $\theta'(t)$ we write them in the form $\{\widetilde{\varphi}'(t), \theta'(t)\} = \{\widetilde{\varphi}', \theta'\} \, \mathrm{e}^{\lambda t}$. Substituting this into (S5–S6) we obtain the homogenous system of algebraic equations for the perturbation amplitudes $\widetilde{\varphi}'$ and θ':

$$\widetilde{\varphi}' s_\theta(\lambda + Bc_\psi) + \omega\theta' = 0 \tag{S8}$$

$$-\widetilde{\varphi}'(Ac_\theta + Bs_\psi s_\theta) + \lambda\theta' = 0 \, . \tag{S9}$$

Nontrivial solutions of Eqs. (S8–S9) require that determinant vanishes, yielding the quadratic equation for the increment: $\lambda^2 + \lambda B c_\psi + \omega \left(A \cot\theta + B s_\psi\right) = 0$. Since the high-frequency sync solution is stable, we expect exponential decay of the perturbations. Indeed, for the frequency $A < \omega < \omega_*$, the equation has two negative real roots, while for $\omega_* < \omega < \omega_{s-o} = \sqrt{A^2 + C^2}$ it possesses two complex conjugate roots (with negative real parts). ω_* is determined from vanishing the discriminant $D = B^2 c_\psi^2 - 4\omega(A \cot\theta + B s_\psi) = 0$. At $\omega = A$ one of the roots is zero and at $\omega = \omega_{s-o}$ both roots turn purely imaginary, meaning that in either case, *i.e.*

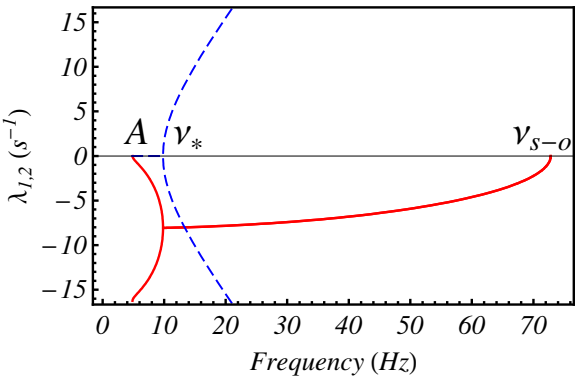

Figure S1: The increment $\lambda_{1,2}$ as a function of driving frequency $\nu = \omega/2\pi$ for the characteristic frequencies: $A/2\pi = 4.9$ Hz, $B/2\pi = 16.2$ Hz and $C/2\pi = 72.6$ Hz. Solid (red) lines stand for the real parts and dashed (blue lines) stand for the imaginary part.

close to tumbling/wobbling transition and to the sync/async transition small orientational fluctuations (e.g. due to thermal noise) are important. For the practically relevant range $\omega_* < \omega < \omega_{s-o}$, the real part of the increment reads

$$\mathrm{Re}\,\lambda = -\frac{B}{2}c_\psi = --\frac{B}{2}\frac{\sqrt{A^2+C^2-\omega^2}}{C} = -\frac{1}{2p}\sqrt{\omega_{s-o}^2-\omega^2}\,, \tag{S10}$$

where $p \equiv \kappa_\perp/\kappa_\parallel > 1$ for a slender propeller. The roots $\lambda_{1,2}$ are shown in Fig. S1 for the values of characteristic frequencies estimated from experiments: $A/2\pi \simeq 4.9$ Hz, $B/2\pi \simeq 16.2$ Hz and $C/2\pi \simeq 72.6$ Hz (see the upcoming sections for details). For these values, $\nu_* = \omega_*/2\pi \approx 13.3$ Hz and for $\theta \lesssim \arcsin(A/\omega_*) \approx 20^\circ$ the roots are complex conjugate.

Now we can estimate $\mathrm{Pe}_r^\perp$ using $\tau_{rel} = |\mathrm{Re}\,\lambda|^{-1}$ and $\tau_d = 1/D_r^\perp = \kappa_\perp/\kappa_B T$:

$$\mathrm{Pe}_r^\perp = \frac{\tau_d}{\tau_{rel}} = \frac{\kappa_\parallel\sqrt{\omega_{s-o}^2-\omega^2}}{2\kappa_B T}\,. \tag{S11}$$

Following the same criterion $Pe_r^\perp = 1$ and using Eq. (S2) we arrive at the critical length of *steerable* nanohelix:

$$L_{r*}^\perp = \left(\frac{2\kappa_B T}{\widetilde{\kappa}_\parallel\eta\sqrt{\omega_{s-o}^2-\omega^2}}\right)^{1/3}\,. \tag{S12}$$

Now, given the geometry of the nanohelices and driving frequency one can estimate $L_{r*}^\parallel$

and L_{t*} in Eqs.(S3) and (S4) respectively, while for the estimate of $L^{\perp}_{r\,*}$ in (S12) one would also need the value of the step-out frequency. Comparing the critical lengths corresponding to rotation about the helical axis and of the helical axis , one can tell that for the latter mechanism to be more restrictive, *i.e.* $L^{\perp}_{r*} > L^{\parallel}_{r*}$ one needs $\frac{1}{2}\sqrt{\omega^2_{s-o} - \omega^2} < \omega$, or just $\omega/\omega_{s-o} > 1/\sqrt{5} \approx 0.45$. For the particular example in Fig. S1 it translates into $\nu \gtrsim 32.5$ Hz.

Note that while $L^{\parallel}_{r*}$, $L_{t*} \sim \eta^{-1/3}$, *i.e.* noise can be suppressed by increasing the viscosity of the medium, steerability is not affected by the viscosity, as sufficiently below the step-out frequency $L^{\perp}_{r*} \approx \left(2\kappa_B T/\widetilde{\kappa}_{\parallel}\eta\omega_{s-o}\right)^{1/3}$, where after substituting $\omega_{s-o} \approx C = m_{\perp}H/\kappa_{\parallel}$ and using $\kappa_{\parallel} = \widetilde{\kappa}_{\parallel}\eta(L^{\perp}_{r*})^3$ we obtain a simple condition for steerability of predominantly transversely magnetized nanomotors operating in sync regime:

$$\left(\frac{2\kappa_B T}{m_{\perp}H}\right)^{1/3} \lesssim 1\,. \tag{S13}$$

Re-writing Eq. (S13) in terms of the Langevin parameter $\xi = m_{\perp}H/\kappa_B T$, measuring the relative importance of the magnetic and thermal forces, it would simply yield $\xi > 2$.

Magnetization, anisotropy field and magnetic torques

According to the SQUID measurements of an array of helices grown on wafer the anisotropy field $H_a \simeq 65$ Oe, transverse magnetic moment (perpendicular to the Ni tablet axis) $m_{\perp} \sim 2 \cdot 10^{-14}$ emu and parallel magnetic moment (parallel to the Ni tablet axis) is $m_{\parallel} \sim 0.6 \cdot 10^{-14}$ emu (CGS). Note that a smaller value of $H_a \sim 10$ Oe is typically reported for thin Ni films,[S3] however, a higher value could be a result of shape anisotropy, *i.e.* due to slight elongation of the (ideally circular) Ni-tablet's in-plane cross-section. Let us consider the tablet as a mono-domain magnetic particle. The effective value of the in-plane anisotropy constant K reads[S3]

$$K = 2\pi\Delta n M_s^2\,. \tag{S14}$$

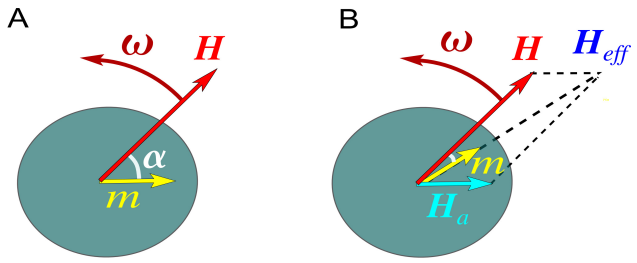

Figure S2: The schematic view of slightly elongated Ni-tablet in-plane cross-section with infinite (A) and finite (B) value of magnetic anisotropy.

where M_s is the saturation magnetization of the magnetic, $\Delta n = n_1 - n_2$ is the difference of the demagnetizing factors along shorter and longer axes, respectively, taken in plane of the tablet. The corresponding value of the anisotropy field H_a reads[S3]

$$H_a = 2K/M_s = 4\pi\Delta n M_s \,. \tag{S15}$$

Let as estimate the aspect ratio $\mathtt{b}/\mathtt{a}$ of the Ni tablet in-plane cross-section corresponding to the measured anisotropy field. We use $M_s = 480$ Oe for the saturation magnetization of Ni and $H_a = 65$ Oe, which results in $\Delta n = 0.011$. The best estimated diameter of the Ni tablet is $d \approx 70$ nm and the height $h \approx 40$ nm. The difference $\Delta n = 0.011$ corresponds to elliptic in-plane cross-section with semi-axes $\mathtt{a} = d/2 + \delta$ and $\mathtt{b} = d/2 - \delta$, where $\delta = 0.6$ nm, *i.e.* , $\mathtt{b}/\mathtt{a} \approx 0.966$. The values of the demagnetizing factors have been taken for the three-axial ellipsoid with semi-axes $h/2$, $\mathtt{a}$ and $\mathtt{b}$ and calculated following.[S4] Note that the measured value is a mean averaged over many helices grown on wafer, while anisotropy field H_a of individual helices may scatter due to shape variance.

The experimentally measured value $m_\perp$ can be compared to a theoretical estimate $m \sim M_s V$, where V is the volume of the Ni-tablet. Approximating the tablet's volume by that of an oblate spheroid, $V \approx \frac{\pi}{6} d^2 h$, with $d \approx 70$ nm and $h \approx 40$ nm, we readily obtain $m \sim 4.9 \cdot 10^{-14}$ emu, that agrees quite well with the value $m_\perp \sim 2 \cdot 10^{-14}$ emu.

Note that the amplitude of the actuating field in the experiment, $H = 100$ Oe, is larger

than the measured anisotropy field $H_a \approx 65$ Oe. To understand the effect of a strong driving field $H > H_a$ let us consider two limiting cases corresponding to (A) infinite ($H \ll H_a$) and (B) finite ($H \gtrsim H_a$) magnetic anisotropy, as depicted schematically in Fig. S2. In case (A) the magnetic moment $\boldsymbol{m}$ is fixed with the particle (for simplicity shown to align with the easy axis). In the sync hi-frequency rotation regime the external field $\boldsymbol{H}$ runs ahead of the propeller's magnetic moment $\boldsymbol{m}$ by an angle $\alpha < 90^{\circ}$ [S1] resulting in the magnetic torque exerted on the propeller

$$\boldsymbol{L}_m^{(A)} = \boldsymbol{m} \times \boldsymbol{H}. \tag{S16}$$

In the case (B) the situation is different: the magnetic moment possesses the same absolute value m, however, it is aligned with the effective magnetic field $\boldsymbol{H}_{eff} = \boldsymbol{H} + \boldsymbol{H}_a$ where $\boldsymbol{H}_a$ is directed along the magnetic easy axis,

$$\boldsymbol{m} = m\frac{\boldsymbol{H}_{eff}}{|\boldsymbol{H}_{eff}|}\,. \tag{S17}$$

Thus in case (B) the magnetic torque takes a form:

$$\boldsymbol{L}_m^{(B)} = \boldsymbol{m} \times \boldsymbol{H} = m\frac{\boldsymbol{H}_a \times \boldsymbol{H}}{|\boldsymbol{H} + \boldsymbol{H}_a|} \lesssim m\frac{\boldsymbol{H}_a \times \boldsymbol{H}}{H} = m\boldsymbol{H}_a \times \boldsymbol{h}\,, \tag{S18}$$

where $\boldsymbol{h} = \boldsymbol{H}/H$ is a unit vector of the applied field.

Let us compare Eqs. (S16) and (S18). It is seen that for sufficiently strong magnetic field the magnetic torque L_m^B saturates, *i.e.* , does not depend on the magnetic field amplitude. Moreover, the ratio $L_m^{(A)}/L_m^{(B)} \approx H/H_a$. Therefore, working with magnetic field $H > H_a$ does not yield re-magnetizing of the particle, but only results in re-orientation of the magnetic moment $\boldsymbol{m}$. The theory of the previous section corresponding to the synchronous actuation of the nanohelix with *fixed* remanent magnetization still applies, however, not all of the power of external magnetic field is exploited since at $H > H_a$ the torque $\boldsymbol{L}_m^{(B)}$ saturates and becomes insensitive to the external field amplitude. Therefore, the magnetic torque exerted

on nanohelices in this case should be replaced by

$$m_\perp H \to m_\perp H_a \,. \tag{S19}$$

For instance, in strong fields $H > H_a$, the step-out frequency will have the form $\omega_{s-o} \approx C = m_\perp H_a/\kappa_\parallel$.

When the frequency of the driving field $\omega > \omega_{s-o}$ and its amplitude $H > H_a$, the dynamic re-magnetizing of the nanohelices, or so-called rotational hysteresis,[S5] takes place. The value of the magnetic torque exerted on a nanohelix in Eq. (S19) should then be replaced by

$$m_\perp H_a \to m_\perp H_a \left(\frac{\omega}{\omega_{s-o}} - \sqrt{\frac{\omega^2}{\omega_{s-o}^2} - 1} \right). \tag{S20}$$

This regime is analogous to the async regime, but the origin of the step-out is of magnetic not of hydrodynamic nature.

Viscous resistances and step-out frequency

The nanohelices used in experiments have the total length (chiral part plus head) of $L \approx 400$ nm, pitch $P \approx 100$ nm and width $2(R + r) \approx 120$ nm. The filament radius roughly estimated from the micrograph is $r \approx 27$ nm and the helical radius $r \approx 33$ nm, so that $R/r \approx 1.2$, leading to a helical pitch angle $\Theta = \tan^{-1}(2\pi R/P) \approx 64^\circ$. The length of the head ~ 90 nm and its width ~ 70 nm, so that the aspect of the propeller is estimated as $\epsilon = 120/400 \simeq 0.30$ (with head) and $\epsilon = 120/310 \simeq 0.39$ (only the chiral part). These values correspond to a helix with 3.6 turns (with the head) or 2.8 turns (without the head). The 3.6-turn helix will be used for estimating rotational resistances $\widetilde{\kappa}_\parallel$, $\widetilde{\kappa}_\perp$, while the 2.8-turn helix will be used for the estimate of the coupling resistance coefficient $\widetilde{\mathcal{B}}_\parallel$. The particle-based computations (see Ref. S1 for details) yield $\widetilde{\kappa}_\parallel \simeq 0.178$, $\widetilde{\kappa}_\perp \simeq 0.796$ and $\widetilde{\mathcal{B}}_\parallel \simeq 0.0112$.

The approximate values of rotational resistance coefficients $\widetilde{\kappa}_\parallel$, $\widetilde{\kappa}_\perp$ can also be obtained

using the exact results for a prolate spheroid embedding the helix. For a prolate spheroid with the semi-axes a and b, we have[S6] $\kappa_\parallel = 2\eta V n_\perp^{-1}$, $\kappa_\perp = 2\eta V \frac{a^2+b^2}{a^2 n_\parallel + b^2 n_\perp}$, where $V = \frac{4}{3}\pi a b^2$ is the spheroid volume, $n_\parallel$ and $n_\perp = (1 - n_\parallel)/2$ are the depolarizing factors of the spheroid. Thus,

$$\widetilde{\kappa}_\parallel = \frac{\pi}{3}\epsilon^2 n_\perp^{-1} \ , \quad \widetilde{\kappa}_\perp = \frac{\pi}{3}\epsilon^2 \frac{1+\epsilon^2}{n_\parallel + \epsilon^2 n_\perp} \ , \tag{S21}$$

where $\epsilon = b/a < 1$ is the aspect ratio of the spheroid. Defining eccentricity $e = \sqrt{1-\epsilon^2}$ the depolarizing factor along the symmetry axis reads[S4] $n_\parallel = \frac{1-e^2}{e^3}\left(\frac{1}{2}\ln\frac{1+e}{1-e} - e\right)$. Substituting the aspect ratio $\epsilon = 1/3.33 \simeq 0.3$ of the 3.6-turn helix into Eqs. (S21) yields $\widetilde{\kappa}_\parallel \approx 0.207$, $\widetilde{\kappa}_\perp \approx 0.755$, in a close agreement with the results of the particle-based calculations (*i.e.* compare to $\widetilde{\kappa}_\parallel \simeq 0.178$, $\widetilde{\kappa}_\perp \approx 0.796$).

Using the estimated values of $\widetilde{\kappa}_\parallel = 0.178$, $\widetilde{\kappa}_\perp = 0.796$ together with $H_a = 65$ Oe, $m_\perp = 2 \cdot 10^{-14}$ emu and $m_\parallel \sim 0.6 \cdot 10^{-14}$ emu, yields the three characteristic frequencies of nanohelices in 25 cP glycerol-water solution, $A/2\pi = m_\parallel H_a / 2\pi\widetilde{\kappa}_\perp \eta L^3 \simeq 4.9$ Hz, $B/2\pi = m_\perp H_a / 2\pi\widetilde{\kappa}_\perp \eta L^3 \simeq 16.2$ Hz and $C/2\pi = m_\perp H_a / 2\pi\widetilde{\kappa}_\parallel \eta L^3 \simeq 72.6$ Hz. Thus, the corresponding step-out frequency

$$\nu_{s-o} = \frac{\sqrt{A^2 + C^2}}{2\pi} \approx \frac{C}{2\pi} \approx 73 \text{ Hz} \, .$$

is in an excellent agreement to the experimental observations showing some decrease of the propulsion speed at the actuating frequency of 80 Hz.

Minimal size of externally actuated nanomotors

Now let us estimate the effect of the noise in experiments with nanohelices. We assume high-frequency synchronous regime[S1] for frequencies below the step-out frequency that we estimated as $\nu_{s-o} \approx 73$ Hz. In water ($\eta = 1$ cP) for the actuating frequency $\nu = 50$ Hz we find using Eqs. (S3) and (S4) that $L_{r*}^\parallel \approx 1,060$ nm and $L_{t*} \approx 420$ nm. These estimates

support the experimental findings indicating that thermal fluctuations hinder propulsion of the nanohelices in water. However, in glycerol-water solution with higher viscosity $\eta = 25$ cP for the same operating conditions we find $L_{r*}^{\parallel} \approx 360$ nm and $L_{t*} \approx 140$ nm, so that thermal noise is not dominating the motion of the 400 nm–long nanomotors in accord with the experimental observations. Note that Eq. (S3) estimating the effect of the thermal fluctuations on forced rotation of the nanohelix about its axis is more restrictive than Eq. (S4), estimating retardation of the forward propulsion, as generally $\widetilde{\mathcal{B}}_{\parallel} \ll \widetilde{\kappa}_{\parallel}$. However, unless $L > L_{t*}$, some forward propulsion should be observed, even if forced rotation is hindered by the noise, *i.e.* even if $L < L_{r*}^{\parallel}$. However, when $L \lesssim L_{t*}$, the forward motion will be hindered. For the lowest frequency of $\nu = 25$ Hz used in experiments (see Tab. 1 in the main text) with glycerol-water solution ($\eta = 25$ cP) we find that $L_{r*}^{\parallel} \approx 450$ nm and $L_{t*} \approx 180$ nm, indicating that forward propulsion is feasible in accord with experimental observations.

To verify the steerability condition in Eq. (S13) we calculate the Langevin parameter,

$$\xi = \frac{m_{\perp} H_a}{\kappa_B T} \approx 32 \gg 2 \, ,$$

indicating that nanohelices are steerable.

Propulsion Experiments

Video 1

Propulsion of a nano-screw at a frequency of 50 Hz and a magnetic field strength of 100 Oe, in a glycerol-water mixture with a viscosity of 25 cP over a time of 2:50 min. The video is sped up 5x. The number in the upper left displays the time, the red arrow shows the direction of propulsion set by the magnetic field. The scale bar is 10 μm.

Video 2

Propulsion of an ensemble of nano-screws through a solution of 5 mg/mL HA at a frequency of 50 Hz and a magnetic field strength of 100 Oe, over a time of 2:32 min. The video is sped up 5x. The number in the upper left displays the time, the red arrow shows the direction of propulsion set by the magnetic field. The scale bar is 10 μm.

References

(S1) K. I. Morozov and A. M. Leshansky, The Chiral Magnetic Nanomotors. *Nanoscale*, 2014, **6**, 1580–1588.

(S2) S. Tottori, L. Zhang, F. Qiu, K. K. Krawczyk, A. Franco-Obregon and B. J. Nelson, Magnetic Helical Micromachines: Fabrication, Controlled Swimming, and Cargo Transport. *Adv. Mater.*, 2012, **22**, 811–816.

(S3) S. V. Vonsovsky, *Magnetizm*, Wiley, New York 1974.

(S4) L. D. Landau and E. M. Lifshitz, *Electrodynamics of Continuous Media*, 2nd ed., Pergamon Press, Oxford, 1984.

(S5) E. Blums, A. Cebers and M. M. Maiorov. *Magnetic Liquids*; Berlin – New York: de Gruyter, 1997.

(S6) G. B. Jeffrey, The Motion of Ellipsoidal Particles Immersed in a Viscous Fluid. *Proc. R. Soc. London A* 1922, **102**, 161–179.